

# Moving Frames for Heart Fiber Geometry

Emmanuel Piuze<sup>‡</sup>, Jon Spurring<sup>§‡</sup>, and Kaleem Siddiqi<sup>‡</sup>

<sup>‡</sup>School of Computer Science & Centre for Intelligent Machines, McGill University.

<sup>§</sup>Science Center, Department of Computer Science, University of Copenhagen.

**Abstract.** Elongated cardiac muscle cells named cardiomyocytes are densely packed in an intercellular collagen matrix and are aligned to helical segments in a manner which facilitates pumping via alternate contraction and relaxation. Characterizing the geometrical variation of their groupings as cardiac fibers is central to our understanding of normal heart function. Motivated by a recent abstraction by Savadjiev et al. of heart wall fibers into generalized helicoid minimal surfaces, this paper develops an extension based on differential forms. The key idea is to use Maurer-Cartan’s method of moving frames to study the rotations of a frame field attached to the local fiber direction. This approach provides a new set of parameters that are complimentary to those of Savadjiev et al. and offers a framework for developing new models of the cardiac fiber architecture. This framework is used to compute the generalized helicoid parameters directly, without the need to formulate an optimization problem. The framework admits a straightforward numerical implementation that provides statistical measurements consistent with those previously reported. Using Diffusion MRI we demonstrate that one such specialization, the homeoid, constrains fibers to lie locally within ellipsoidal shells and yields improved fits in the rat, the dog and the human to those obtained using generalized helicoids.

**Keywords:** Heart Myofibers, Differential Geometry, Connection Forms, Moving Frames, Diffusion MRI, Generalized Helicoids.

## 1 Introduction

Cardiac myofibers are densely packed in the heart wall and are locally aligned to helical curves [1]. Helices act as geodesics between points in the myocardium and mathematical analyses by Peskin [2] and Horowitz et. al [3] support the view that this alignment is mechanically optimal. As a result, geometric descriptions of cardiac fibers using the helix angle, taken to be the projected angle between the fiber direction and the short-axis plane (see Fig. 1a), are popular in the literature. Several accounts from both small-scale histology and voxel-scale studies based on Diffusion MRI (dMRI) report that along a transmural penetration line from the heart’s outer to inner wall, the helix angle varies smoothly and regularly undergoing a total change in orientation of about  $120^\circ$  [1, 4–7]. The range of the transverse angle, which is the angle formed by a fiber moving away from a plane perpendicular to the transmural direction, is much smaller, about  $\pm 10^\circ$  [4, 8], and is therefore often ignored in the literature.

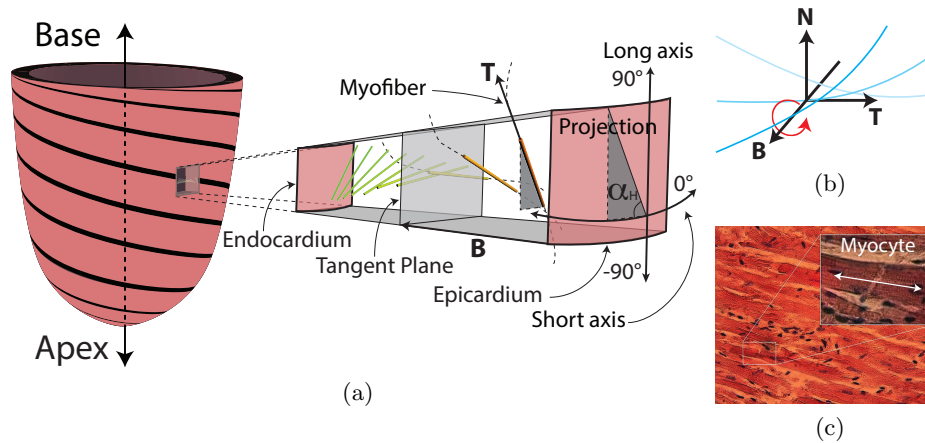


Fig. 1: (1a) The helix angle  $\alpha_H$  is defined as the angle between the short axis of the heart and the projected myofiber orientation in a plane orthogonal to the transmural direction. (1b) The transmural change in the helix angle in the direction  $\mathbf{B}$ , orthogonal to the heart wall tangent plane. (1c) A histological slice of cardiac tissue showing individual elongated cardiomyocytes and their nuclei (dark) in the intercellular collagen network (*adapted from Wikimedia Commons*).

The analysis of myofibers from histological slices is cumbersome and their invasiveness does not easily admit an association with the original intact three-dimensional geometry. Thus, many modern analysis methods work with cardiac fiber orientation data derived from dMRI measurements [4–6, 9, 10]. However, the scale at which current dMRI measurements are made is at least one order of magnitude larger than the length of individual cardiomyocytes [8]. The measured signal therefore reflects the composite behaviour of large groups of cardiac muscle cells within the collagen matrix (Fig. 1c). Savadjiev et al. [11] have recently obtained a promising characterization of the collective geometrical variation of cardiac fibers, using a method derived from texture flow analysis [12]. They arrived at the conclusion that the cardiac fiber directions across three mammalian species – the rat, the canine and the human – are locally described by a particular minimal surface, the generalized helicoid model (GHM).

A limitation of the GHM is that its streamlines lie on a planar manifold in spite that the heart wall is curved (Fig. 1a). The GHM thus captures the variability of cardiac fibers in a plane tangent to the local cardiac wall but not orthogonally to it. Moreover, experimental results have shown that the GHM is only accurate in the immediate neighborhood of a voxel, with fitting errors growing rapidly as the neighborhood in which the fits are applied is increased [11]. Motivated by these observations, this paper develops an extension by attaching a local frame field to the fiber and transmural directions and studying the full differential geometry of this moving frame through the Maurer-Cartan connec-

tion one-forms. We show that locally the GHM can in fact be measured directly using a combination of connection forms. We then introduce a sub-class of differential form-based models for which the streamlines lie on ellipsoidal shells or *homeoids* (Section 3.4). Using the same database examined by Savadjiev et al. in [11] we demonstrate that local measurements on homeoids give lower fitting errors than generalized helicoids. We begin by introducing the Maurer-Cartan form in Section 2.

## 2 The Maurer-Cartan Form

We characterize the differential geometry of fibers in the heart wall by measuring the manner in which they turn locally. For this purpose, we construct a frame field  $\mathbf{F}_1, \mathbf{F}_2, \mathbf{F}_3 \in \mathbb{R}^3$ ,  $\mathbf{F}_i \cdot \mathbf{F}_j = \delta_{ij}$ , where  $\delta_{ij}$  is the Kronecker delta, in such a manner that the turning of the frame field characterizes the turning of the fibers. The frame field is expressed as a rotation of the cartesian frame  $[\mathbf{e}_1 \ \mathbf{e}_2 \ \mathbf{e}_3]^T$ ,

$$[\mathbf{F}_1 \ \mathbf{F}_2 \ \mathbf{F}_3]^T = \mathbf{A} [\mathbf{e}_1, \mathbf{e}_2, \mathbf{e}_3]^T, \quad (1)$$

where the attitude matrix  $\mathbf{A} \in \text{SO}(3)$  is a smoothly varying orthonormal matrix, and where the basis vectors  $\mathbf{e}_j$  are treated as symbols such that  $\mathbf{F}_i = \sum_j a_{ij} \mathbf{e}_j$ .

The differential geometry of the fibers is now directly characterized by the attitude transformation. Its differential structure is found to be [13]

$$d \begin{bmatrix} \mathbf{F}_1 \\ \mathbf{F}_2 \\ \mathbf{F}_3 \end{bmatrix} = \begin{bmatrix} d\mathbf{F}_1 \\ d\mathbf{F}_2 \\ d\mathbf{F}_3 \end{bmatrix} = (d\mathbf{A}) \begin{bmatrix} \mathbf{e}_x \\ \mathbf{e}_y \\ \mathbf{e}_z \end{bmatrix} = (d\mathbf{A}) \mathbf{A}^{-1} \begin{bmatrix} \mathbf{F}_1 \\ \mathbf{F}_2 \\ \mathbf{F}_3 \end{bmatrix} = \mathbf{C} \begin{bmatrix} \mathbf{F}_1 \\ \mathbf{F}_2 \\ \mathbf{F}_3 \end{bmatrix}, \quad (2)$$

where  $d$  is the differential operator,  $\mathbf{A}^{-1} = \mathbf{A}^T$ ,  $\mathbf{C} = (d\mathbf{A}) \mathbf{A}^{-1}$  is the Maurer-Cartan form, and where for simplicity the notation  $d\mathbf{F}_i = \sum_j c_{ij} \mathbf{F}_j$  is used. The Maurer-Cartan matrix is skew symmetric, i.e.,  $\mathbf{C} = -\mathbf{C}^T$ . Hence it has at most 3 independent, non-zero elements:  $c_{12}$ ,  $c_{13}$ , and  $c_{23}$ . Each  $c_{ij}$  is a one-form in  $\mathbb{R}^3$  that can be contracted on a vector  $\mathbf{v} = [v_1, v_2, v_3]^T \in \mathbb{R}^3$  to yield the initial rate of turn of  $\mathbf{F}_i$  towards  $\mathbf{F}_j$  when moving in the direction of  $\mathbf{v}$ . We denote this contraction  $c_{ij}\langle \mathbf{v} \rangle$ , which is found to be  $c_{ij}\langle \mathbf{v} \rangle = \nabla_{\mathbf{v}} \mathbf{F}_i \cdot \mathbf{F}_j|_{\mathbf{x}}$ , where  $\mathbf{x} \in \mathbb{R}^3$  is a point in the fiber field and  $\nabla_{\mathbf{v}} \mathbf{F}_i$  is the covariant derivative of  $\mathbf{F}_i$  in the direction  $\mathbf{v}$ . Thus,

$$c_{ij}\langle \mathbf{v} \rangle = [F_{j1} \ F_{j2} \ F_{j3}] \begin{bmatrix} \partial_x F_{i1} & \partial_y F_{i1} & \partial_z F_{i1} \\ \partial_x F_{i2} & \partial_y F_{i2} & \partial_z F_{i2} \\ \partial_x F_{i3} & \partial_y F_{i3} & \partial_z F_{i3} \end{bmatrix} \begin{bmatrix} v_1 \\ v_2 \\ v_3 \end{bmatrix}, \quad (3)$$

where the components of the frame vectors are enumerated as  $\mathbf{F}_i = [F_{i1}, F_{i2}, F_{i3}]^T$  and where  $\partial_x \equiv \frac{\partial}{\partial x}$  is used to denote partial derivatives. Since we are interested in studying the change of the frame field in the direction of its basis vectors we study the contractions  $c_{ijk} \equiv c_{ij}\langle \mathbf{F}_k \rangle$ . Note that the frame field  $\mathbf{F}_1, \mathbf{F}_2, \mathbf{F}_3$

has 3 degrees of freedom. Since this field roams a 3-dimensional space, a linear model of the spatial change of the frame field must have 9 degrees of freedom, which are embodied in  $e_{ijk}$ .

The abstraction and the comprehensiveness in the one-form description of the geometrical behavior of a frame field can be harnessed to develop models that are descriptive of the variability of cardiac fiber orientations across multiple species. The next section introduces a class of fiber models based on one-forms and reintroduces the GHM of [11] as a planar approximation to the complete one-form parameterization.

### 3 Measures on a Discrete Fiber Frame Field

We analyze hearts represented as diffusion MRI volumes embedded in 3D rectangular lattices with coordinates  $\mathbf{x} = xe_1 + ye_2 + ze_3 = [x, y, z]^T \in \mathbb{Z}^3$ . A tangent vector  $\mathbf{T}$  is identified as the principal eigenvector of the diffusion tensor field. Consistency in  $\mathbf{T}$  amongst voxel neighbours is enforced by adopting an adaptive cylindrical coordinate system. The centroid  $\mathbf{c}_z$  of the chamber within each short-axis slice  $s_z$  is first determined.  $\mathbf{T}(\mathbf{x})$  is then made to turn clockwise with respect to that centroid as follows:

$$\mathbf{T}(\mathbf{x}) \rightarrow \text{sign}((\mathbf{T} \times (\mathbf{x} - \mathbf{c}_z)) \cdot \mathbf{l}(s_z)) \mathbf{T}(\mathbf{x}), \quad (4)$$

where  $\mathbf{l}(s_z)$  is the local approximation of the heart's long-axis. For all the hearts that we consider,  $\mathbf{l}(s_z)$  approximately coincides with the world's  $z$  axis. In the spirit of [11], the heart transmural direction  $\hat{\mathbf{B}}$  is estimated as the gradient vector of a distance transform produced as follows: a) the binary image (mask) of the heart is closed using mathematical morphological operations, b) the closest distance to the heart wall is evaluated at every point, c) the gradient of the distance transform is computed, and finally d) the skeletal points of colliding fronts are removed and interpolated by thresholding the magnitude of the gradient vectors. The normals  $\hat{\mathbf{B}}$  are then aligned to point from outer to inner wall. With  $\mathbf{T}$  and  $\hat{\mathbf{B}}$  we specify a local frame

$$\mathbf{F}_1 = \frac{\mathbf{T}}{\|\mathbf{T}\|}, \quad \mathbf{F}_2 = \mathbf{N} = \mathbf{F}_3 \times \mathbf{F}_1, \quad \mathbf{F}_3 = \mathbf{B} = \frac{(\hat{\mathbf{B}} - (\hat{\mathbf{B}} \cdot \mathbf{T})\mathbf{T})}{\|\hat{\mathbf{B}} - (\hat{\mathbf{B}} \cdot \mathbf{T})\mathbf{T}\|}, \quad (5)$$

where  $\mathbf{B}$  is the part of  $\hat{\mathbf{B}}$  orthogonal to  $\mathbf{T}$ . From here on, we will use the symbols  $\mathbf{T}$ ,  $\mathbf{N}$ , and  $\mathbf{B}$  interchangeably with the corresponding symbols  $\mathbf{F}_j$ . We will also refer to the local plane spanned by  $\mathbf{T}$  and  $\mathbf{N}$  as the *tangent plane*.

#### 3.1 One-Form Intuition

One-form contractions  $c_{ijk}$  can be interpreted as the amount of turning of  $\mathbf{F}_i$  towards  $\mathbf{F}_j$  in the direction  $\mathbf{F}_k$ . For example,  $c_{TNB}$  describes a transmural rotation of  $\mathbf{T}$  towards  $\mathbf{N}$ , as shown in Fig. 1b.  $c_{ijk}$  were computed at each

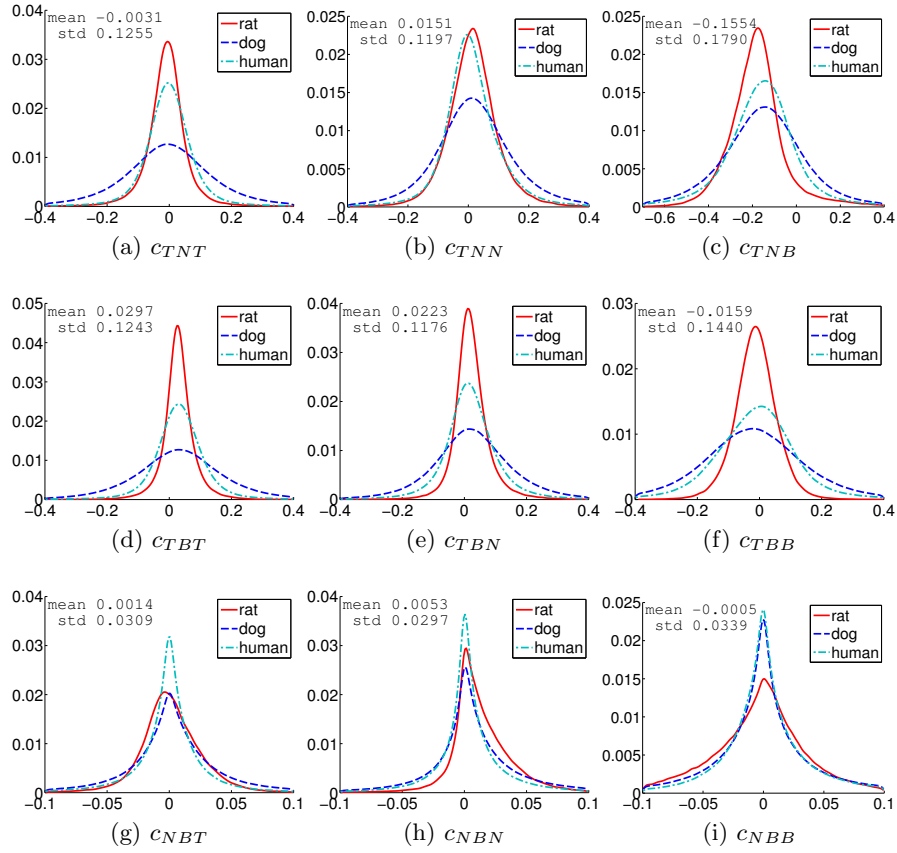


Fig. 2: Histogram of  $c_{ijk} \equiv c_{ij} \langle \mathbf{F}_k \rangle$  for 3 species: rat, human, dog. All measures have been normalized such that the horizontal axis is in mm.

voxel from the discrete fiber frame field combined with (3). Histograms for three species (rat, canine, human) are shown in Fig. 2 and illustrate statistics on the local turning of the frame field. The rotations of  $\mathbf{T}$  towards  $\mathbf{N}$ ,  $c_{TN} \langle \mathbf{F}_k \rangle$ , are intimately linked to the curvature parameters of the GHM in [11]. These rotations intuitively describe the manner in which fibers turn in the tangent plane of the heart:  $c_{TNT}$ , shown in Fig. 2a, describes their tangential curvature,  $c_{TNN}$ , shown in Fig. 2b, their fanning in the tangent plane, and  $c_{TNB}$ , shown in Fig. 1b, their transmural turning or equivalently the rate of change of the *helix angle*. This is arguably the most salient variation of the cardiac fibers. The rotations of  $\mathbf{T}$  towards  $\mathbf{B}$ ,  $c_{TB} \langle \mathbf{F}_k \rangle$ , express the turning of the fibers towards the inner wall:  $c_{TBT}$  effectively measures the first the local curvature of the heart,  $c_{TBN}$  describes a twisting of the tangent plane and the rate of change of the *transverse angle*, and  $c_{TBB}$  measures a fanning or thickening of the local fiber

population away from the tangent plane, towards the inner wall. As shown in Fig. 2g–2i, the remaining rotations of  $\mathbf{N}$  towards  $\mathbf{B}$ ,  $c_{NB}\langle \mathbf{F}_k \rangle$ , are an order of magnitude smaller in all 3 directions which indicate that the frame field axis  $\mathbf{N}$  is constrained within the local tangent plane.  $c_{NBT}$  measures a twisting of the tangent plane,  $c_{NBN}$  the second curvature of the heart wall, and  $c_{NBB}$  a transmural fanning or thickening.

### 3.2 The One-Form Model

The Maurer-Cartan form extrapolates the local shape to first order as

$$\tilde{\mathbf{T}}_h = \mathbf{T} + c_{TN}\langle \mathbf{h} \rangle \mathbf{N} + c_{TB}\langle \mathbf{h} \rangle \mathbf{B} \quad (6)$$

$$\begin{aligned} &= \mathbf{T} + (c_{TNT} \mathbf{h} \cdot \mathbf{T} + c_{TNN} \mathbf{h} \cdot \mathbf{N} + c_{TNB} \mathbf{h} \cdot \mathbf{B}) \mathbf{N} \\ &\quad + (c_{TBT} \mathbf{h} \cdot \mathbf{T} + c_{TBN} \mathbf{h} \cdot \mathbf{N} + c_{TBB} \mathbf{h} \cdot \mathbf{B}) \mathbf{B}, \end{aligned} \quad (7)$$

where  $\mathbf{h}$  is an offset from the point at which the frame is expressed and  $\tilde{\mathbf{T}}_h$  represents the predicted direction of this neighbor by the one-form extrapolation to first-order approximation. As in [11], we construct an error measure by computing the average angular difference between the measured and predicted directions in an isotropic neighborhood  $\mathcal{N}_i$ ,

$$e(\mathcal{N}_i) = \frac{1}{|\mathcal{N}_i|} \sum_{\mathbf{h} \in \mathcal{N}_i} \arccos \left( \mathbf{T}_h \cdot \frac{\tilde{\mathbf{T}}_h}{\|\tilde{\mathbf{T}}_h\|} \right), \quad (8)$$

where  $|\mathcal{N}_i| = i^3$  for odd  $i \in \mathbb{Z}$  and  $\mathbf{T}_h$  is the true neighbor's measured direction. The associated errors of fit for different species are shown in Fig. 3. Diffusion MRI noise and resolution, heart size, and underlying fiber geometry are factors that account for the error disparity across different species. We delay further analysis of these errors to Section 4, where they will be compared against those of the other models we will introduce next.

### 3.3 The Generalized Helicoid as a Subset of the One-Form Model

The generalized helicoid model of Savadjiev et al. [11] expresses the local fiber direction in a plane tangent to the heart wall. Within the local coordinate frame,

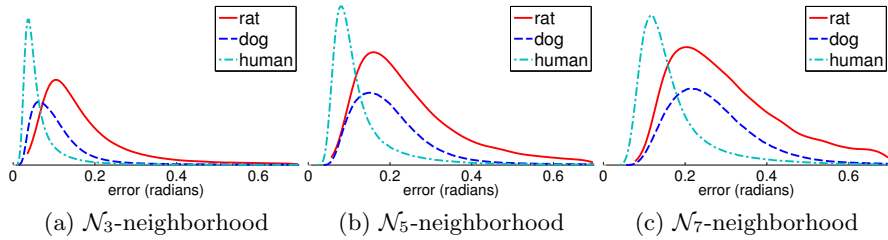


Fig. 3: One-form extrapolation error for neighborhoods of size  $|\mathcal{N}_i| = 3^3, 5^3, 7^3$ .

the fiber direction at a point  $\mathbf{x} = x_T \mathbf{T} + x_N \mathbf{N} + x_B \mathbf{B} \in \mathbb{R}^3$  is given as the angle

$$\theta(\mathbf{x}, K_T, K_N, K_B) = \arctan\left(\frac{K_T x_T + K_N x_N}{1 + K_N x_T - K_T x_N}\right) + K_B x_B, \quad (9)$$

where  $K_* \in \mathbb{R}$  are the GHM curvature parameters. Direct calculations show that a frame field spanned by  $\mathbf{T}(\theta)$ ,  $\mathbf{N}(\theta)$ ,  $\mathbf{B}(\theta)$  has instantaneous turning given by  $c_{TN}\langle\mathbf{T}(\theta)\rangle = K_T$ ,  $c_{TN}\langle\mathbf{N}(\theta)\rangle = K_N$ ,  $c_{TN}\langle\mathbf{B}(\theta)\rangle = K_B$ , with the remaining one-forms all being zero. The GHM parameters can thus be estimated directly using (3) and the GHM model may be evaluated directly using (7) and central differences as an alternative to the generative model (9). To compare these 2 representations, the parameter vector  $\mathbf{K} = (K_T, K_N, K_B)$  of the GHM was estimated at each voxel using a standard Nelder-Mead optimization scheme. The problem was formulated as the selection of the parameters  $\mathbf{K}$  which minimize an extension of (8), where  $\tilde{\mathbf{T}}_h \rightarrow \tilde{\mathbf{T}}_h(\mathbf{K}) = (\cos \theta, \sin \theta, 0)$  and  $\theta = \theta(\mathbf{K})$  as given by (9). Results for the fitting error and a comparison with the one-forms are shown in Fig. 4. The results indicate that the one-form model is able to capture the GHM's parameterization accurately and that it consistently yields lower errors. Note that in addition to an improved fitting method – continuous rather than discrete – we estimate heart wall normals slightly differently than is done in the original work [11]. Consequently, our GHM parameters estimates are more precise and still support the overall shape distribution reported. From here on, we will therefore consider the GHM using its one-form approximation, which we refer to as the *ghm-form*.

The following section introduces a differential model, the *homeoid*, that can also be expressed using a subset of the one-forms, and has the advantage that it is intuitively connected to the large-scale structure of the heart by enforcing the ellipsoidal topology of the local tangent plane.

### 3.4 The Generalized Helicoid on an Ellipsoid is a Homeoid

The calculations of the previous section can be applied to model fibers with smoothly varying fiber orientations, such that the differential operations are well defined. Motivated by evidence that fibers wind around the heart wall while remaining approximately parallel to the tangent plane to the wall at each location [1, 5, 9], we now consider a specialization to the case where the fibers lie locally on *thin homeoids*, which are shells composed of two concentric and similar ellipsoids.

As introduced in Section 2, the Maurer-Cartan form has only 3 independent one-forms:  $c_{TN}\langle\cdot\rangle$ ,  $c_{TB}\langle\cdot\rangle$ , and  $c_{NB}\langle\cdot\rangle$  with 3 associated spatial degrees of freedom, for a total of 9 possible combinations. Working with the intuition given in Section 3.2 of each  $c_{ijk}$ , this is a convenient space to develop models of fiber geometry. For example, in Section 3.3 we showed that for the GHM only  $c_{TN}\langle\mathbf{T}\rangle$ ,  $c_{TN}\langle\mathbf{N}\rangle$ , and  $c_{TN}\langle\mathbf{B}\rangle$  are non-zero. Based on a general description of the cardiac fiber architecture as collections of fibers that i) vary smoothly and ii) are locally constrained to the tangent space of smooth and orthogonal surfaces to the heart wall, the following contractions of 1-forms must occur:

$$c_{TN}\langle\mathbf{T}\rangle = \alpha, c_{TN}\langle\mathbf{N}\rangle = \beta, c_{TN}\langle\mathbf{B}\rangle = \gamma, c_{TB}\langle\mathbf{B}\rangle \approx 0, c_{NB}\langle\mathbf{B}\rangle \approx 0. \quad (10)$$

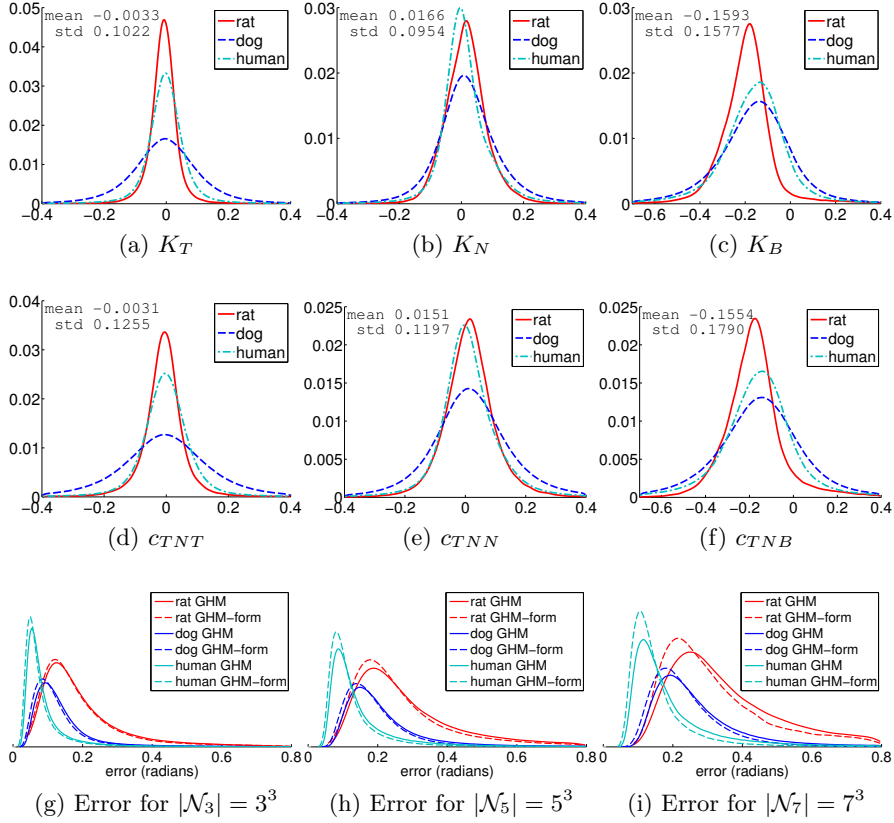


Fig. 4: Rows 1 and 2 compare the one-form approximation to the GHM for the neighborhood  $\mathcal{N}_3$ . Horizontal axes are given in radians/mm. Row 3 compares the error of each model as a function of  $\mathcal{N}_i$ .

Locally, these fibers lie in the tangent plane of a thin homeoid. The parameter fields  $\alpha$ ,  $\beta$ , and  $\gamma$  are introduced as the curvature parameters of the fibers.  $c_{NBB}$  must be zero otherwise fibers could move in and out of the local tangent plane and our hypothesis ii) would not be satisfied. The remaining contractions specify the shape of the homeoid and we have

$$c_{TB}\langle \mathbf{T} \rangle = \frac{1}{\rho_1}, c_{NB}\langle \mathbf{N} \rangle = \frac{1}{\rho_2}, c_{TB}\langle \mathbf{N} \rangle = 0, c_{NB}\langle \mathbf{T} \rangle = 0, \quad (11)$$

where  $\rho_1$  and  $\rho_2$  are the radii fields of the osculating ellipsoid. Using (7), the model can be employed to extrapolate the orientation of fibers in the neighborhood of a point  $\mathbf{x}$ . Constraints given by (10) and (11) are satisfied by enforcing the nullity of  $c_{TBN}$  and  $c_{TBB}$  such that we obtain

$$\tilde{\mathbf{T}}_h = \mathbf{T} + c_{TN}\langle \mathbf{h} \rangle \mathbf{N} + (c_{TBT} \mathbf{h} \cdot \mathbf{T}) \mathbf{B}. \quad (12)$$

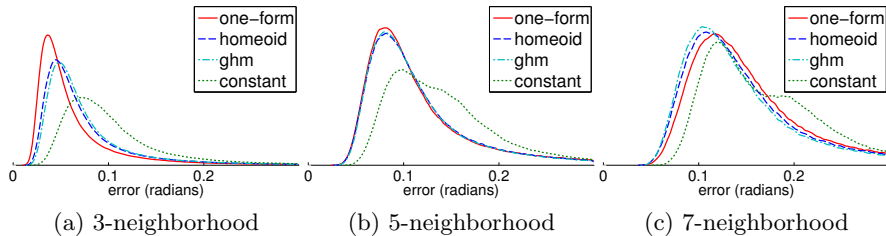


Fig. 5: Human error of fit for the different models analyzed in this paper. Results are shown for isotropic voxel neighbourhoods of size  $3^3$ ,  $5^3$ , and  $7^3$ .

## 4 Model Space Comparison

The analytical models of fiber geometry described so far vary in their parametric complexity. The one-form, homeoid and generalized helicoid models respectively have 9, 5, and 3 parameters. We introduce the *constant* model which will serve as a base-line to which the remaining models can be compared. This parameter-free model simply assumes  $\tilde{\mathbf{T}}_h = \mathbf{T}$  in (7). To compare the different models in terms of their fitting accuracy, we have evaluated each  $c_{ijk}$  on the human data set using first-order central differences on  $3^3$  neighbors. We then used these one-forms to extrapolate each model using (7) and (8) in isotropic neighborhoods  $\mathcal{N}_i$  where  $|\mathcal{N}_i| = i^3$  for  $i = 3, 5, 7, 9$ . Fig. 5 shows a distribution of the error of fit in the human dataset for the different models across increasingly large voxel neighborhoods. Error generally increases with neighborhood size but the relative performance of each model is difficult to assess. We therefore fitted a log-normal distribution to each error plot and show the resulting log-normal mode  $e^{\mu - \sigma^2}$  and mean  $e^{\mu + \frac{1}{2}\sigma^2}$  as a function of neighborhood size in Fig. 6. As expected, the constant model provides an upper bound on the error of fit and is a measure of the smoothness in the data. The one-form model has the lowest error of fit when the neighborhood size reflects the scale at which central differences were computed but behaves poorly for larger neighborhood sizes, which we attribute to local overfitting. On the other hand, the ghm-form and the homeoid models are well-behaved for all neighborhood sizes and differ only slightly from one another. In Section 3.4 we showed that their extrapolated  $\tilde{\mathbf{T}}_h$  axis only differs by the  $c_{TBT}$  one-form which is a measure of the curvature of the heart wall. For the human, this value is small and therefore the two models should be very similar. The rat hearts is smaller in size and therefore has larger per voxel curvature. In this case Table 1 shows that the homeoid is a better fit.

A moving frame in  $\mathbb{R}^3$  has 3 degrees of freedom of which 2 are captured by the error vector  $\mathbf{T} - \tilde{\mathbf{T}}_h$ : the angular difference  $e(\mathcal{N})$  between dMRI orientations and extrapolations specified by (8), and a rotation  $\phi$  about  $\mathbf{T}$ . The third DOF is the rotation  $\psi$  of  $\mathbf{N}$  about  $\mathbf{T}$ .  $\psi$  strongly depends on the calculations of  $\hat{\mathbf{B}}$  and much less on the direct measurements. In contrast to the GHM, the homeoid

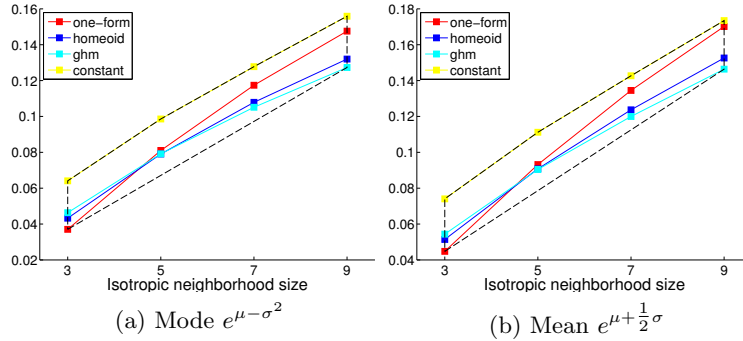


Fig. 6: Log-normal fits of the human heart extrapolation error. The mode and mean describe the precision of the fit and the skewness of the distribution.

model considers this angle. However, since we focus on the direct measurement of the fiber geometry given by  $\mathbf{T}$ , we leave further investigation of  $\psi$  as future work.  $\phi$  can be obtained by projecting  $\mathbf{T} - \tilde{\mathbf{T}}_h$  onto the local  $\mathbf{NB}$  plane and measuring its angle with respect to the frame axis  $\mathbf{N}$ :  $\phi = \arctan \frac{(\mathbf{T} - \tilde{\mathbf{T}}_h) \cdot \mathbf{B}}{(\mathbf{T} - \tilde{\mathbf{T}}_h) \cdot \mathbf{N}}$ , i.e., values of  $\phi = (0, \pi)$  and  $(\frac{\pi}{2}, \frac{3\pi}{2})$  respectively indicate alignment with the frame vectors  $\mathbf{N}$  and  $\mathbf{B}$ . Fig. 5 showed the marginal distributions of  $e(\mathbf{x}, \mathcal{N})$  for various neighborhood sizes and Fig. 7 shows the marginal distributions of  $\phi$ . In Fig. 8 we show the joint histogram of these marginal distributions for the human heart and for the 4 different models in a  $3^3$  extrapolation neighborhood. Note that the error along  $\phi$  is negligible when  $e$  is small. The spread of  $\phi$  measures the rotation of the local  $\mathbf{NB}$  plane, which for the one-form model results in overfitting for larger neighborhood sizes.

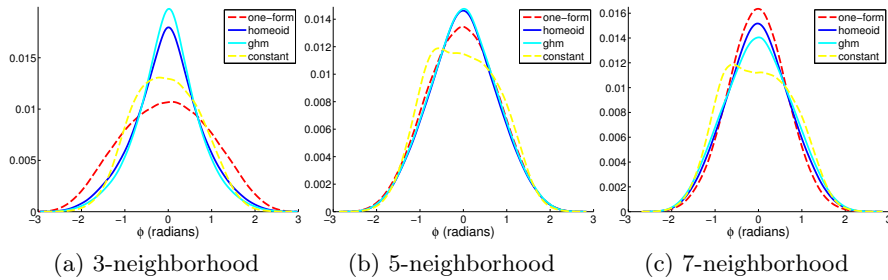


Fig. 7: Rotational angle  $\phi$  of the different models analyzed in this paper for the human heart in isotropic voxel neighbourhoods of size  $3^3$ ,  $5^3$ , and  $7^3$ .

$ N_i $		Rat (mode, mean)	Dog (mode, mean)	Human (mode, mean)
$3^3$	one-form	<b>0.093, 0.113</b>	<b>0.076, 0.092</b>	<b>0.039, 0.054</b>
	homeoid	0.094, 0.115	0.085, 0.102	0.046, 0.063
	ghm-form	0.099, 0.118	0.089, 0.106	0.050, 0.066
	constant	0.163, 0.181	0.110, 0.128	0.070, 0.090
$5^3$	one-form	0.146, 0.175	0.157, 0.181	0.085, 0.112
	homeoid	<b>0.145, 0.173</b>	0.152, 0.176	0.085, 0.112
	ghm-form	0.150, 0.175	<b>0.147, 0.171</b>	<b>0.085, 0.111</b>
	constant	0.271, 0.286	0.156, 0.178	0.109, 0.135
$7^3$	one-form	0.202, 0.239	0.220, 0.251	0.124, 0.161
	homeoid	<b>0.200, 0.234</b>	0.202, 0.235	0.117, 0.152
	ghm-form	0.206, 0.237	0.189, 0.221	<b>0.114, 0.147</b>
	constant	0.389, 0.402	<b>0.189, 0.215</b>	0.141, 0.172

Table 1: Extrapolation error in radians for each species, differential model, and neighborhood  $\mathcal{N}_i$  from the mode  $e^{\mu-\sigma^2}$  and the mean  $e^{\mu+(1/2)\sigma^2}$  of log-normal fits. The model with the best performance is selected as the one that minimizes the mode (and the mean to resolve multiplicity), and is highlighted for each  $\mathcal{N}_i$ .

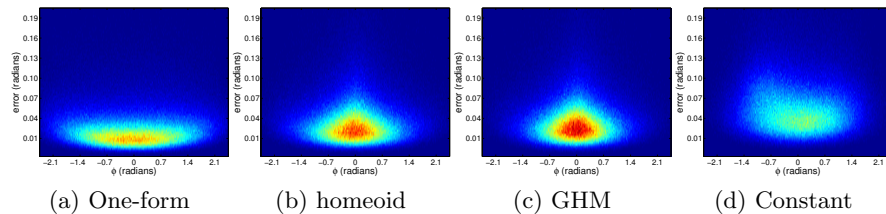


Fig. 8: Joint histogram of the angular errors  $e$  and  $\phi$  in the human heart for different models. Results are shown for an isotropic  $3^3$  neighborhood with minimum values colored in dark blue and maximum values in dark red.

In summary, we have shown that the one-form model yields the lowest fitting error for small neighborhoods and that the homeoid model is as accurate as or better than the GHM depending on the per-voxel curvature of the heart wall.

## 5 Conclusion

We have presented a framework for analyzing cardiac fiber geometry based on the method of Maurer-Cartan’s moving frames. Using this framework we were able to make predictions of the differential geometry of fibers that corroborate previously reported values. We proposed the homeoid as an extension to the GHM for characterizing cardiac geometry. We demonstrated that this model a) lowers the error of fit across multiple species, b) offers a trade-off between the geometrical comprehensiveness of the complete one-form model and the minimality of the GHM, and finally c) incorporates two important parameters,  $\rho_1 = c_{TBT}^{-1}$

and  $\rho_2 = c_{TBN}^{-1}$  which measure the curvature of the local tangent plane. Our framework provides intuitive tools for reasoning about the differential geometry of cardiac muscle and opens up many possibilities. Further work includes exploring the behavior of cardiac fibers in their one-form description, possibly across a greater number of species, for assessing the existence of cardiac sheets and uncovering descriptors of heart pathology and fiber remodeling. Future work also includes the consideration of higher-order and scale-space approaches to differentiation, the study of different cardiac frame fields, and a study of the relative information content stored in individual one-forms.

## References

1. Streeter, D.D.: Gross morphology and fiber geometry of the heart. In R.M., B., N., S., eds.: Handbook of Physiology, Section 2. The Heart. Williams and Wilkins, New York, NY, USA (1979) 61–112
2. Peskin, C.S.: Mathematical aspects of heart physiology. Technical report, Courant Institute of Math. Sciences, New York University, New York, NY, USA (1975)
3. Horowitz, A., Perl, M., Sideman, S.: Geodesics as a mechanically optimal fiber geometry for the left ventricle. *Basic. Res. Cardiol.* **88 Suppl 2** (1993) 67–74
4. Geerts, L., Bovendeerd, P., Nicolay, K., Arts, T.: Characterization of the normal cardiac myofiber field in goat measured with mr-diffusion tensor imaging. *Am. J. Physiol.: Heart and Circ. Physiol.* **283** (2002) H139–145
5. Beg, M.F., Helm, P.A., McVeigh, E.M., Miller, M.I., Winslow, R.L.: Computational cardiac anatomy using mri. *Magn. Reson. Med.* **52** (2004) 1167–1174
6. Chen, J., Liu, W., Zhang, H., Lacy, L., Yang, X., Song, S.K., Wickline, W.A., Yu, X.: Regional ventricular wall thickening reflects changes in cardiac fiber and sheet structure during contraction: quantification with diffusion tensor mri. *Am. J. Physiol.: Heart and Circ. Physiol.* **289** (2005) H1898–1907
7. Streeter, D., Bassett, D.: An engineering analysis of myocardial fiber orientation in pig’s left ventricle in systole. *The Anatomical Record* **155**(4) (2005) 503–511
8. LeGrice, I.J., Smail, B.H., Chai, L.Z., Edgar, S.G., Gavin, J.B., Hunter, P.J.: Ventricular myocyte arrangement and connective tissue architecture in the dog. *Am. J. Physiol.: Heart. and Circ. Physiol.* **269** (1995)
9. Rohmer, D., Sitek, A., Gullberg, G.T.: Reconstruction and visualization of fiber and laminar structure in the normal human heart from ex vivo diffusion tensor magnetic resonance imaging (dtmri) data. *Invest. Radiol.* **42**(11) (2007) 777–789
10. Lombaert, H., Peyrat, J., Croisille, P., Rapacchi, S., Fanton, L., Clarysse, P., Delingette, H., Ayache, N.: Statistical analysis of the human cardiac fiber architecture from dt-mri. *Functional Imaging and Modeling of the Heart* (2011)
11. Savadjiev, P., Strijkers, G.J., Bakermans, A.J., Piuze, E., Zucker, S.W., Siddiqi, K.: Heart wall myofibers are arranged in minimal surfaces to optimize organ function. *Proc. Natl. Acad. Sci. USA.* **109**(24) (2012) 9248–9253
12. Ben-Shahar, O., Zucker, S.W.: The perceptual organization of texture flow: A contextual inference approach. *IEEE TPAMI* **25**(4) (2003)
13. Koenderink, J.: Solid shape. Volume 2. Cambridge Univ Press (1990)